photonics

MDPI

Article

Polarization Fading Noise Suppression in Phase-Sensitive OTDR Using Variational Mode Decomposition

Ruotong Mei [1], Weidong Bai [1,2], Xinming Zhang [1,2], Junhong Wang [1,2], Yu Wang [3,4] and Baoquan Jin [1,4,*]

[1] College of Electronic Information Engineering, Taiyuan University of Technology, Taiyuan 030024, China; 2023002593@link.tyut.edu.cn (R.M.); baiweidong0225@link.tyut.edu.cn (W.B.); 2024521580@link.tyut.edu.cn (X.Z.); 2023310305@link.tyut.edu.cn (J.W.)
[2] Key Laboratory of Advanced Transducer and Intelligent Control Systems (Ministry of Education), Taiyuan University of Technology, Taiyuan 030024, China
[3] College of Robotics Science and Engineering, Taiyuan University of Technology, Taiyuan 030024, China; wangyu@tyut.edu.cn
[4] Shanxi Key Laboratory of Intelligent Measurement and Control for Coal Mine Electromechanical Equipment, Taiyuan University of Technology, Taiyuan 030024, China
* Correspondence: jinbaoquan@tyut.edu.cn

Abstract

To address the polarization fading noise in coherent detection phase-sensitive optical time-domain reflectometry (Φ-OTDR) for distributed low-frequency vibration sensing, a Φ-OTDR sensing scheme integrating polarization diversity reception and the variational mode decomposition (VMD) algorithm is proposed. The mechanism of polarization fading induced by fiber birefringence and external perturbations is systematically analyzed. A signal–noise mathematical model for polarization diversity reception is established, and the adaptive decomposition capability of the VMD algorithm for non-stationary phase signals is elaborated. This scheme can accurately separate the additional noise introduced by polarization diversity reception from the target low-frequency vibration signals. Experimental results demonstrate that, compared with the single-path detection scheme, the proposed method eliminates the amplitude attenuation of beat frequency signals caused by polarization mismatch at the optical path level. Meanwhile, it effectively suppresses both the additional noise introduced by polarization diversity and the low-frequency phase drift resulting from unstable laser frequency. It achieves precise phase restoration of vibration signals excited at 50 Hz under three typical sensing distances of 5 km, 10 km, and 30 km. Additionally, it successfully restores low-frequency vibration signals as low as 0.6 Hz at the sensing distance of 30 km.

Keywords: phase-sensitive optical time-domain reflectometer; polarization fading; polarization diversity reception; variational mode decomposition; distributed optical sensing; vibration detection

Check for updates

Received: 30 March 2026
Revised: 20 April 2026
Accepted: 21 April 2026
Published: 24 April 2026

Copyright: © 2026 by the authors. Licensee MDPI, Basel, Switzerland. This article is an open access article distributed under the terms and conditions of the Creative Commons Attribution (CC BY) license.

1. Introduction

The distributed optical fiber sensing technology, with its outstanding anti-electromagnetic interference capability and distributed full boundary monitoring feature, can achieve precise perception of multiple physical quantities such as sound waves, vibrations, temperature and axial strain of optical fibers [1–3]. It demonstrates great application value in key fields such as safety inspection of petroleum pipelines, health monitoring of large-scale infrastructural facilities, security warning [4] and geological disaster detection. As a pivotal

technique within the domain of distributed optical fiber sensing, the phase-sensitive optical time-domain reflectometer (Φ-OTDR) has emerged as a key enabler for long-range, high-precision vibration monitoring across diverse engineering scenarios, converts standard communication optical fibers into distributed acoustic sensor arrays by using Rayleigh scattering, and has become the mainstream solution for long-distance and high-sensitivity vibration monitoring.

However, the traditional single-path detection Φ-OTDR system encounters a core performance bottleneck in practical applications, namely polarization fading. The inherent birefringence of the sensing fiber, combined with external environmental perturbations, can induce stochastic evolution in the polarization characteristics of both the signal light and the local oscillator reference light [5]. When the polarization states of the two are mismatched, the intensity of the beat frequency signal decreases, and in extreme cases, when the polarization states are completely orthogonal, the signal completely disappears, making the system unable to extract vibration information [6,7]. This significantly increases the false alarm rate and false positive rate, severely restricting the stability and reliability of the system. The problem of signal attenuation caused by the random evolution of polarization states limits the engineering application of Φ-OTDR technology in long distances and dynamic complex environments. How to effectively suppress polarization fading and ensure stable signal amplitude has become a core research topic that urgently needs to be addressed in this field.

To overcome this performance bottleneck, scholars both at home and abroad have conducted extensive research on polarization fading suppression. The existing technologies mainly cover active polarization control, digital signal processing, fiber structure optimization, and adaptive algorithm denoising. However, there are still limitations, such as poor architecture compatibility and insufficient amplitude suppression or phase demodulation capabilities. For example, C Chen et al. proposed a polarization feedback control and chaotic particle swarm optimization method for asymmetric dual Mach-Zehnder interferometer systems, which successfully reduced the localization error to 54% of its initial magnitude over a 72.14 km transmission link [8]. However, this solution relies on hardware-level polarization controllers and phase modulators, resulting in a high system complexity and limited compatibility with the Φ-OTDR architecture. X Wu et al. proposed a digital scheme based on polarization diversity virtual coherence, achieving synchronous fading noise suppression and phase demodulation through virtual cross coherence, obtaining a positioning signal-to-noise ratio (SNR) of 27.14 dB and a phase demodulation SNR of 47.88 dB in distributed vibration sensing, providing a simplified integrated solution for the Φ-OTDR system [9]. However, this scheme has a high algorithm complexity, and the long-distance sensing performance has not been verified [10–12]. F Sandah et al. quantitatively analyzed the polarization-dependent effect in FBG-assisted direct detection Φ-OTDR, verifying that spun fibers can effectively alleviate polarization attenuation [13]. However, this solution relies on passive polarization suppression by fiber selection and is limited to the FBG-assisted architecture, lacking active processing methods [14]. T Mou et al. proposed a mixed polarization scheme in OFDR systems, reducing the polarization angle fluctuation to 2.81°, achieving a sensitivity of −145 dB and a Rayleigh scattering SNR of 32 dB [15]. However, it is only applicable to optical frequency domain reflection measurements and cannot be directly transferred to the Φ-OTDR time-domain system.

In conclusion, although the existing polarization fading suppression techniques can ensure a certain degree of signal amplitude stability, problems such as the additional noise introduced by polarization diversity reception, low-frequency phase distortion caused by laser frequency drift [16], etc., have not been effectively resolved. This leads to a degraded system signal-to-noise ratio, difficulty in accurately restoring low-frequency

vibration signals, and an inability to simultaneously meet the multiple requirements of high stability, high SNR, and high-precision demodulation. This paper proposes a Φ-OTDR system scheme that combines polarization diversity reception with the variational mode decomposition (VMD) algorithm. Based on the polarization diversity structure, which effectively alleviates polarization fading at the optical path level, the VMD algorithm is innovatively introduced to adaptively process the non-stationary phase signals after demodulation. Unlike the limitations of Empirical Mode Decomposition (EMD), which suffers from mode aliasing, Wavelet Transform, which relies on preset basis functions, and traditional filtering, which is prone to introducing phase distortion, VMD is based on the variational framework to enforce the effective separation of different frequency components. It can adaptively determine the center frequency and bandwidth of each mode without the need for preset basis functions. It can decompose nonlinear and non-stationary phase signals into multiple modal components with independent center frequencies [17–19], accurately separating low-frequency phase drift, circuit noise, and additional noise from polarization diversity, and achieving efficient noise reduction while retaining the details of the real vibration signals to the greatest extent. The paper systematically analyzes the principle responsible for polarization fading, the polarization diversity signal and noise model, and the decomposition and noise reduction principle of the VMD algorithm [20,21] and constructs a complete theoretical system. Experimental findings demonstrate that this scheme can effectively restore the vibration phase signals at different distances and frequencies, significantly suppress the noise base, optimize the power spectral density (PSD), and achieve a high signal-to-noise ratio and high-precision phase demodulation in long-distance, low-frequency, and sub-Hertz vibration detection. This scheme provides an efficient and stable solution for the Φ-OTDR system to simultaneously address the problems of polarization fading and noise degradation.

2. Methods

2.1. Polarization Fading Mechanism

Taking the polarization diversity receiving architecture of the coherent detection Φ-OTDR system as the research object, the complex amplitude E_s of the Rayleigh backscattered light field detected at the optical fiber front end can be expressed as:

$$E_S = \sum_{k=1}^{N} A_k \exp\left(-\alpha \frac{c\tau_k}{n_f}\right) \exp[j(\omega + \Delta\omega)(t - \tau_k)] U\left(\frac{t - \tau_k}{W}\right) \quad (1)$$

Among them, N denotes the total count of scattering bodies within the sensing optical fiber, c stands for the velocity of light in vacuum, α represents the fiber transmission loss coefficient, and n_f corresponds to the refractive index of the optical fiber. Specifically, A_k and τ_k denote the amplitude and temporal delay associated with the kth Rayleigh backscattering event, ω is the central angular frequency of the laser source, and $\Delta\omega$ refers to the frequency shift induced by the acousto-optic modulator. $U(t/W)$ is a rectangular window function. When $0 \leq t/W \leq 1$, this function is 1; otherwise, it is 0.

The Rayleigh Backward Scattering (RBS) light is projected onto two orthogonal polarization axes, respectively. Based on the different propagation rates of the light on these two axes, it can be classified into a P-axis and an S-axis, generating two orthogonal components E_{sp} and E_{ss}. Throughout the fiber-optic sensing procedure, the combined effects of external environmental perturbations and the inherent birefringent structure of the fiber lead to random evolution of the sensing light's polarization state among elliptical, linear, and circular polarization modes. As a consequence, both the amplitude and phase of E_{sp} and E_{ss} exhibit stochastic fluctuations over time t.

In the coherent detection structure of Φ-OTDR, the reference light E_{LO} generated by the narrow linewidth laser can be expressed as:

$$E_{LO} = B\cos(\omega t + \phi_0) \tag{2}$$

The powers of the reference light projected onto the P-axis and the S-axis are E_{LOP} and E_{LOS}, respectively. Similar to the signal light, E_{LOP} and E_{LOS} also change randomly over time.

After the reference light and the Rayleigh backscattered light are frequency-modulated, the resulting frequency-modulated signal is as shown in Formula (3):

$$E = (E_{LO} + E_S)^2 = E_{LO}^2 + E_S^2 + 2E_{LO}E_S \tag{3}$$

The beat frequency signals corresponding to the P-axis and S-axis components are designated as E_P and E_S, respectively. When the polarization matching coefficient of either axis approaches zero, the intensity of the associated beat frequency signal E_P and E_S will also decay to nearly zero, which is defined as the occurrence of polarization fading in the system [5].

2.2. Polarization Diversity Mechanism

The principle of polarization diversity reception is as follows: At the receiving end, a polarization beam splitter is used to separate the local oscillator light and the signal light into two beams with mutually orthogonal polarization states. Then, frequency division is performed in these two polarization directions [9]. After photoelectric detection, the signals are added together. Since squaring-law demodulation is performed before the addition, between the two orthogonal polarization states, the phase influence can be eliminated.

The signal light, the light signal passing through the 45° junction and the local oscillator light are respectively:

$$\begin{gathered} E_S = A\cdot\cos\theta_m\cdot\cos(\omega_0 t + \varphi_m)\overline{X} + A\cdot\sin\theta_m\cdot\cos(\omega_0 t + \varphi_m + \delta_m)\overline{Y} \\ E_{LO} = 2B\cos\theta_m\cdot\cos(\omega_l t + \omega_L)\overline{X} \\ E_L = B\cos(\omega_l t + \omega_L)\overline{X} + B\cos(\omega_l t + \omega_L)\overline{Y} \end{gathered} \tag{4}$$

Here, θ_m represents the field strength of the signal light in the $\overline{XY}$ axis, and δ_m is the phase discrepancy between the two optical axes. The output beam after passing through the coupler is:

$$\begin{gathered} E_1 = \frac{1}{\sqrt{2}}\left[A\cos\theta_m\cdot\cos(\omega_0 t + \varphi_m) + B\cos\left(\omega_l t + \varphi_L + \frac{\pi}{2}\right)\right]\overline{X} \\ + \frac{1}{\sqrt{2}}\left[A\sin\theta_m\cdot\cos(\omega_0 t + \varphi_m + \delta_m) + B\cos\left(\omega_l t + \varphi_L + \frac{\pi}{2}\right)\right]\overline{Y} \end{gathered} \tag{5}$$

$$\begin{gathered} E_2 = \frac{1}{\sqrt{2}}\left[A\cos\theta_m\cdot\cos\left(\omega_0 t + \varphi_m + \frac{\pi}{2}\right) + B\cos(\omega_l t + \varphi_L)\right]\overline{X} \\ + \frac{1}{\sqrt{2}}\left[A\sin\theta_m\cdot\cos\left(\omega_0 t + \varphi_m + \delta_m + \frac{\pi}{2}\right) + B\cos(\omega_l t + \varphi_L)\right]\overline{Y} \end{gathered} \tag{6}$$

Assuming that the balanced receiver is in an ideal matching state, the output photocurrent is:

$$\begin{gathered} I_x \propto 2AB\cos\theta_m\sin(\Delta\omega\cdot t + \Delta\varphi) \\ I_y \propto 2AB\sin\theta_m\cos(\Delta\omega\cdot t + \Delta\varphi + \delta_m) \end{gathered} \tag{7}$$

Among them, $\Delta\omega = \omega_1 - \omega_2$, $\Delta\varphi = \varphi_1 - \varphi_m$.

The polarization diversity receiving scheme requires special processing in the Φ-OTDR system. Due to the distributed reflection, the received signals θ_m and δ_m at different distances from the reference arm are different. This will cause Equation (7) to become:

$$\begin{aligned} I_x &\propto \sum A(n \cdot \Delta r) \cos\theta_m(n \cdot \Delta r) \sin(\Delta\omega \cdot t + \Delta\varphi(n \cdot \Delta r)) \\ I_y &\propto \sum A(n \cdot \Delta r) \sin\theta_m(n \cdot \Delta r) \sin(\Delta\omega \cdot t + \Delta\varphi(n \cdot \Delta r) + \delta(n \cdot \Delta r, t)) \end{aligned} \tag{8}$$

$\Delta\varphi(r)$ represents the phase difference caused by different reflection points, and $\delta(r,t)$ represents the difference in birefringence effect due to different reflection points and the surrounding environment of the fiber under test. It is worth noting that $\delta(r,t)$ has a lower frequency and will not have a significant impact on the spectrum. To eliminate the polarization fading caused by $\theta_m(r)$, the corresponding terms in Equation (8) can be squared and added together to eliminate the influence of $\theta_m(r)$. Obviously, it is impossible to achieve polarization diversity reception through analog circuits without introducing cross-interference. Based on the Φ-OTDR system, which only cares about the amplitude information in the frequency domain, a digital system can be considered to implement polarization diversity reception. The signals I_x and I_y obtained by the photodetector are respectively subjected to a fast Fourier transform to obtain amplitude spectra $|I_x(f)|$ and $|I_y(f)|$. Then, by squaring and adding the $|I_x(f)|$ and $|I_y(f)|$ corresponding to each frequency point, the influence can be eliminated in the frequency domain.

Figure 1a shows the original beat frequency curve obtained by dual-channel acquisition under the polarization diversity structure. Figure 1b is a local magnification of the two beat frequency signals. From the figure, when the P-channel signal experiences a decline at 6.816 km, the S-channel signal does not show a significant decline. When the S-channel signal experiences a decline at 6.823 km, the P-channel signal does not experience a decline. The above results indicate that the two Rayleigh backscattering (RBS) signals with orthogonal polarization states are less likely to simultaneously experience a decline in space, thereby verifying the effectiveness of the polarization diversity structure in suppressing signal decline.

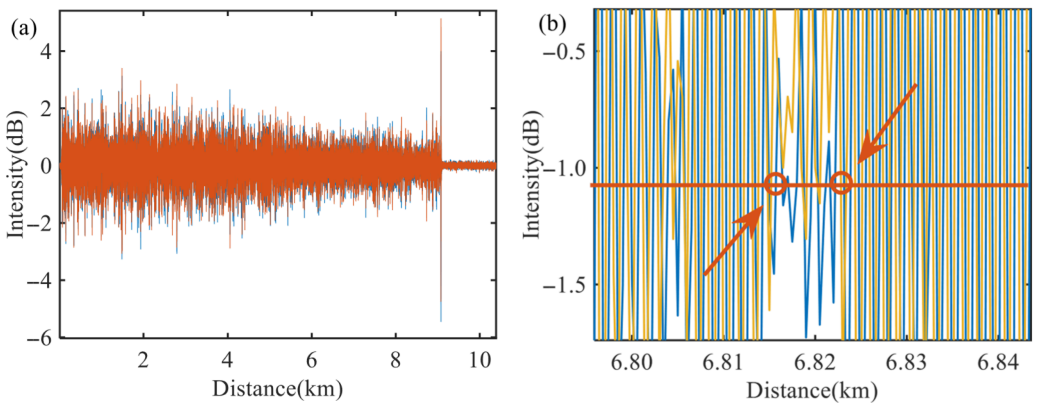


Figure 1. Original biphasic frequency curve and local magnification of the biphasic frequency curve. (**a**) original biphasic frequency curve; (**b**) local magnified view of the bimodal frequency curve near 6.82 km.

2.3. Noise Reduction Mechanism of VMD

Suppose the single-path detection signal is:

$$I_1(t) = s(t) + n_1(t) \tag{9}$$

Here, $s(t)$ is the useful signal and $n_1(t)$ is zero-mean Gaussian white noise.

In polarization diversity reception, the signals of the two orthogonal polarization channels can be expressed as:

$$\begin{cases} I_x(t) = s_x(t) + n_x(t) \\ I_y(t) = s_y(t) + n_y(t) \end{cases} \tag{10}$$

Among them, the useful signal satisfies $s_x(t) = s(t)cos\theta_m$ and $s_y(t) = s(t)sin\theta_m$. The two noise channels $n_x(t)$ and $n_y(t)$ are independent and identically distributed zero-mean Gaussian white noises, satisfying $E[n_x(t)] = E[n_y(t)] = 0$, $E\left[n_x^2(t)\right] = E\left[n_y^2(t)\right] = \sigma_n^2$, $E[n_x(t)n_y(t)] = 0$.

The core operation of polarization diversity is to square and add the two signals together to eliminate the influence of the polarization angle θ_m. Therefore, there is

$$I_{out} = I_x^2(t) + I_y^2(t) \tag{11}$$

Expanding the signal term yields:

$$I_{out}(t) = s_x^2(t) + s_y^2(t) + n_x^2(t) + n_y^2(t) + 2s_x(t)n_x(t) + 2s_y(t)n_y(t) \tag{12}$$

The signal consists of signal terms, noise self-multiplication terms and signal–noise cross-terms. When calculating the signal-to-noise ratio for a single-path detection, the following result is obtained:

$$SNR_1 = \frac{E\left[s^2(t)\right]}{\sigma_n^2} \tag{13}$$

When the squares of the two paths of polarization diversity are added together, the SNR is obtained:

$$SNR_{OUT} = \frac{e\left[s^2(t)\right]}{2\sigma_n^2 + 4E[s^2(t)]\sigma_n^2} \tag{14}$$

Obviously, $SNR_{OUT} < SNR_1$, representing the noise power after polarization diversity, significantly increases and the SNR decreases. Therefore, in this paper, the VMD algorithm is employed to process the demodulation phase curve in order to solve the noise problem caused by polarization diversity.

Variational mode decomposition (VMD) is an adaptive, completely non-recursive signal-processing technique rooted in modal variational principles, initially introduced by Dragomiretskiy K et al. The core mechanism of the VMD algorithm lies in solving a constrained variational problem, which enables the decomposition of the original input signal into K discrete modal components according to their respective frequency characteristics. Here, K denotes the predefined number of intrinsic mode function (IMF) components, and each extracted IMF corresponds to a distinct central frequency band, which will continuously change during the iterative process [17]. The ultimate goal is to decompose the original signal into K modal numbers, and the bandwidth and center frequency of all IMF components are obtained through a cumulative search of the variational model to achieve the best solution [18].

The original signal can be decomposed into K modes, and the resulting IMF components are individual amplitude-modulated and frequency-modulated signals, which can be expressed as follows:

$$u_k(t) = A_k(t)\cos(\phi_k(t)) \tag{15}$$

In the formula, $A_k(t)$ represents the instantaneous amplitude and $\Phi_k(t)$ represents the phase.

In the variational construction process of the VMD algorithm, an analytical signal framework is first established by introducing a unit impulse signal, and the Hilbert transform is used to calculate the unilateral spectrum for each intrinsic mode function (IMF). The core objective is as follows: On the one hand, by using the Hilbert transform, the real-valued mode components are converted into analytic signals. Essentially, this involves performing the Hilbert transform on the real-valued signal to obtain its orthogonal components and then combining these with the original real-valued signal to form a complex-form analytic signal. This completely eliminates the negative frequency components that are symmetrical to the positive frequency components in the frequency spectrum of the real-valued signal, resulting in a unilateral amplitude spectrum that only contains the positive frequencies. This avoids the energy aliasing and center frequency estimation errors caused by the bilateral spectrum, ensuring the accurate estimation of the center frequency of each mode. On the other hand, the ideal frequency domain characteristics of the unit impulse signal are utilized to construct a frequency domain constraint structure with compact support, making each intrinsic mode appear as a narrowband signal around the center frequency in the frequency domain. This ensures that the components are separated in the frequency domain and do not interfere with each other.

Based on this, the spectra of each intrinsic mode function are modulated by an exponential phase factor, and their center frequencies are successively shifted to the baseband range. Finally, the multi-component signal is adaptively separated, regularized, and expressed in the frequency domain. The final spectral expression is:

$$H_k = \left[\left(\delta(t) + \frac{j}{\pi t}\right) u_k(t)\right] e^{-j\omega t} \tag{16}$$

To determine the bandwidth of each modal function signal, the constrained variational model can be obtained through the following equation:

$$\begin{cases} \min\limits_{\{u_k\},\{\omega_k\}} \left\{ \sum\limits_{k=1}^{K} \left\| \partial_t \left[\left(\delta(t) + \frac{j}{\pi t}\right) u_k(t) \right] e^{-j\omega t} \right\|_2^2 \right\} \\ s.t. \sum\limits_{k=1}^{K} u_k(t) = f(t) \end{cases} \tag{17}$$

In this formula, u_k represents the K individual IMF components of the signal, and ω_k represents the center frequency of each IMF.

To acquire the optimal solution of the aforementioned variational model, the Lagrange operator λ and the penalty factor α are introduced into Equation (17) to construct the augmented Lagrange function. The constrained optimization problem corresponding to the variational model is converted into an unconstrained form, and the derived governing equation is given as follows:

$$\begin{aligned} \mathcal{L}(\{u_k\},\{\omega_k\},\lambda) = \alpha \sum_{k=1}^{K} \left\| \partial_t \left[\left(\delta(t) + \frac{j}{\pi t}\right) u_k(t) \right] e^{-j\omega_k t} \right\|_2^2 \\ + \left\| f(t) - \sum_{k=1}^{K} u_k(t) \right\|_2^2 + \langle \lambda(t), f(t) - \sum_{k=1}^{K} u_k(t) \rangle \end{aligned} \tag{18}$$

For the augmentation of the Lagrange expression, update them using the alternating method of multiplication operators, and simultaneously update the multiplication opera-

tors. Stop the update process when the following condition is met, and obtain the iterative equations for u_k, ω_k, and $\hat{\lambda}$ as follows:

$$\begin{cases} \hat{u}_k^{(n)}(\omega) = \dfrac{\hat{f}(\omega) - \sum\limits_{i \neq k} \hat{u}_i^{(n)}(\omega) + \dfrac{1}{2}\hat{\lambda}^{(n-1)}(\omega)}{1 + 2\alpha\left(\omega - \omega_k^{(n-1)}\right)^2} \\ \omega_k^{(n)} = \dfrac{\int_0^\infty \omega \left|\hat{u}_k^{(n)}(\omega)\right|^2 d\omega}{\int_0^\infty \left|\hat{u}_k^{(n)}(\omega)\right|^2 d\omega}, \; k \in \{1, 2, 3 \cdots K\} \\ \hat{\lambda}^{(n)}(\omega) = \hat{\lambda}^{(n-1)}(\omega) + \tau\left[\hat{f}(\omega) - \sum\limits_{k=1}^{K} \hat{u}_k^{(n)}(\omega)\right] \end{cases} \tag{19}$$

$$\sum_{k=1}^{K} \left\| \hat{u}_k^{n+1} - \hat{u}_k^n \right\|^2 / \sum_{k=1}^{K} \|\hat{u}_k^n\|^2 < \varepsilon \tag{20}$$

In this formula, $\hat{f}(\omega) - \sum\limits_{i \neq k} \hat{u}_i^{(n)}(\omega)$ represents the residual component, $\hat{u}_k^{n+1}(\omega)$ represents the result after Wiener filtering, performing FFT, $\{u_k(t)\}$ is the real part of the value, and ω_k^{n+1} represents the power spectrum center of this iterative mode function.

In this experiment, the number of modal decompositions K for the VMD algorithm is not a fixed value. Instead, it is adaptively selected based on the spectral complexity of the signal's frequency spectrum under different transmission distances and vibration frequencies: For the double-channel summed phase signals of 0.6 Hz, 0.8 Hz, 1 Hz, 10 Hz, and 50 Hz at a 30 km sensing distance, K = 5, 7, 7, 6, 3 is set respectively; for the 50 Hz vibration signal, K = 5, 4, 3 is set respectively at 5 km, 10 km, and 30 km distances The waveform corresponding to the selected K value is the optimal waveform for phase demodulation, which will be used for further processing in the subsequent steps. This parameter selection fully considers the low-frequency drift, polarization noise, and the degree of aliasing of the target vibration signal under different working conditions, ensuring the effective separation of each frequency component, avoiding modal aliasing, and preventing the introduction of false modes and computational redundancy due to over-decomposition. The remaining parameters are set as follows: the bandwidth constraint penalty factor is set to α = 2000 to achieve optimal noise suppression; the DC component is set to 0; and spectrum initialization is set to init = 1.

At the same time, the algorithm adopts a uniform initialization strategy for the central frequency, avoiding the deviation caused by artificially presetting frequencies, allowing the algorithm to adaptively determine the center frequency of each mode based on the non-stationary and multi-frequency characteristics of the Φ-OTDR phase signal.

In summary, the process of the VMD algorithm is illustrated in the following figure:

Figure 2 illustrates the iterative optimization process of the VMD algorithm. The algorithm initially sets the number of iterations to zero, then enters the main loop, and successively processes the preset K modal components. In each iteration step, the kth IMF and its corresponding center frequency are updated separately, and the Lagrange multipliers are updated simultaneously to enhance the degree of satisfaction with the constraint conditions. The algorithm determines whether to terminate the iteration by checking whether the given convergence condition is met: if it is, the current K IMF components obtained through decomposition are output; otherwise, the iteration count is incremented by 1, and the update process is repeated in a loop until the convergence criterion is reached.

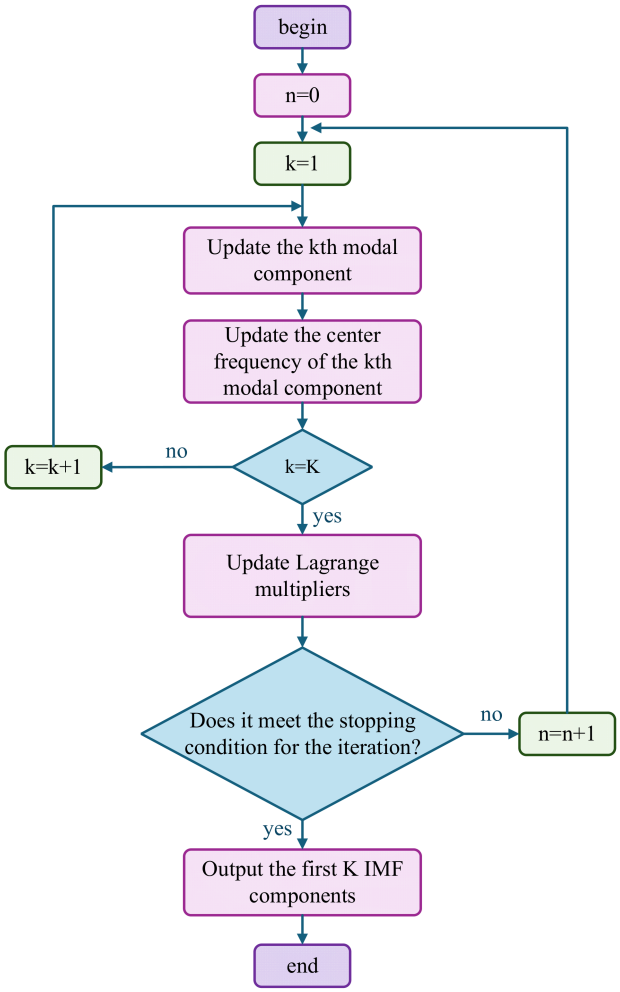


Figure 2. Flowchart of VMD algorithm processing.

Figure 3 illustrates the polarization diversity receiving optical path configuration of the coherent detection Φ-OTDR system. In this setup, the narrow linewidth laser (Laser) serves as the light source, and its highly coherent output is split by a 99:1 optical coupler (OC3) into 1% of the reference light and 99% of the signal light. The signal light is modulated into a pulse form by an acousto-optic modulator (AOM), amplified by an erbium-doped fiber amplifier (EDFA), filtered by a dense wavelength division multiplexing (DWDM) filter to remove amplified spontaneous emission noise, and then injected into the sensing fiber through port 2 of the fiber circulator. A piezoelectric ceramic transducer (PZT) is set on the sensing fiber to apply external vibration excitation, and the fiber end is connected to an optical isolator (ISO) to eliminate the interference of end-face reflection. The returned Rayleigh backscattering (RBS) light from the sensing fiber is output through port 3 of the fiber circulator, and 1% of the reference light is input separately into two polarization beam splitters (PBS1, PBS2). After separation into orthogonal polarization components, they are then combined with the reference light through a 50:50 optical coupler (OC1, OC2), frequency-locked with the reference light, and sent to a balanced photodetector (BPD) for photoelectric conversion. Finally, the two signals are collected by the data acquisition card (DAQ).

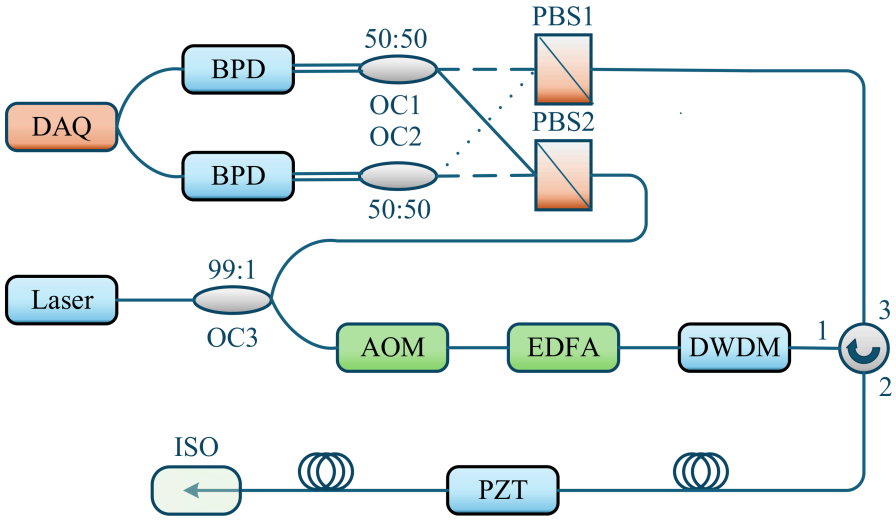


Figure 3. Polarization diversity DAS optical path structure.

The experimental parameters are set as follows: The narrow linewidth laser uses the Koheras Ajustik E15 by NKT Photonics, Birkerød, Denmark, with a central wavelength of 1550 nm, a linewidth of 100 Hz, and an output power of 40 mW; the working frequency offset of the AOM (acoustic-optic modulator) is fixed at 200 MHz, with repetition frequencies of 1 kHz and 200 Hz, and a pulse width of 100 ns; the center wavelength of the dense wavelength division multiplexing (DWDM) filter is 1550 nm; the bandwidth of the balanced photodetector (BPD) is 350 MHz; the sampling rate of the data acquisition system is 1 GS/s. The external vibration excitation uses a low-frequency sine waveform, with an amplitude of 2 V, and includes variable frequency components.

3. Results

3.1. Results and Analysis of Vibration Detection at Different Distances

Figure 4a is a vibration waterfall plot, which visually presents the change in vibration intensity over time. As shown in this figure, at the 13,150 m position where vibration was applied, a significant change in vibration intensity occurred. Figure 4b shows the vibration location curve of the system. This curve is calculated through the differential cumulative average algorithm: Firstly, the original time-space data of the Φ-OTDR is processed through spatial domain differential processing to suppress the system's DC offset, low-frequency noise and interference from non-target areas, highlighting the signal mutation characteristics caused by vibration; then, the differential results are subjected to multi-pulse accumulation and averaging operations along the time dimension to achieve the smooth suppression of random noise and the coherent enhancement of effective vibration signals, and finally, sharp characteristic peaks are formed in the spatial dimension to complete the vibration positioning [21]. As can be seen from the figure, the developed system is capable of accurately identifying the location of the vibration event imposed at the 13,150 m segment of the optical fiber. and the corresponding location signal-to-noise ratio is 24.17 dB.

Figure 5 presents a comparative analysis of the phase recovery outcomes acquired before and after the implementation of the VMD-based optimization algorithm at a vibration frequency of 50 Hz for different sensing distances. Specifically, Figure 5a, Figure 5c, and Figure 5e correspond to the original phase restoration diagrams for sensing distances of 5 km, 10 km, and 30 km, respectively, while Figure 5b, Figure 5d, and Figure 5f represent the phase restoration diagrams for the corresponding sensing distances after optimization using the VMD algorithm. The vibration acquisition time for all cases is 0.3 s. As can be

seen from the figure, the VMD algorithm can accurately restore the phase waveforms under different sensing distances.

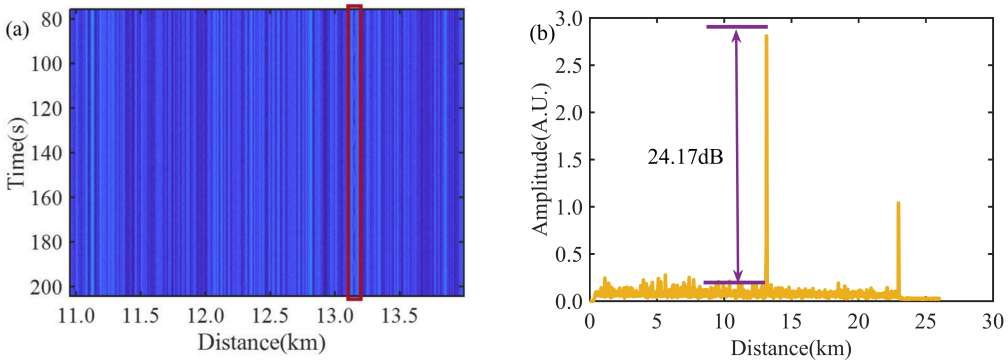


Figure 4. Waterfall plot at the location of the vibration signal and the phase positioning result. (**a**) Waterfall plot, the area enclosed by the red frame represents the location of the vibration; (**b**) phase positioning result.

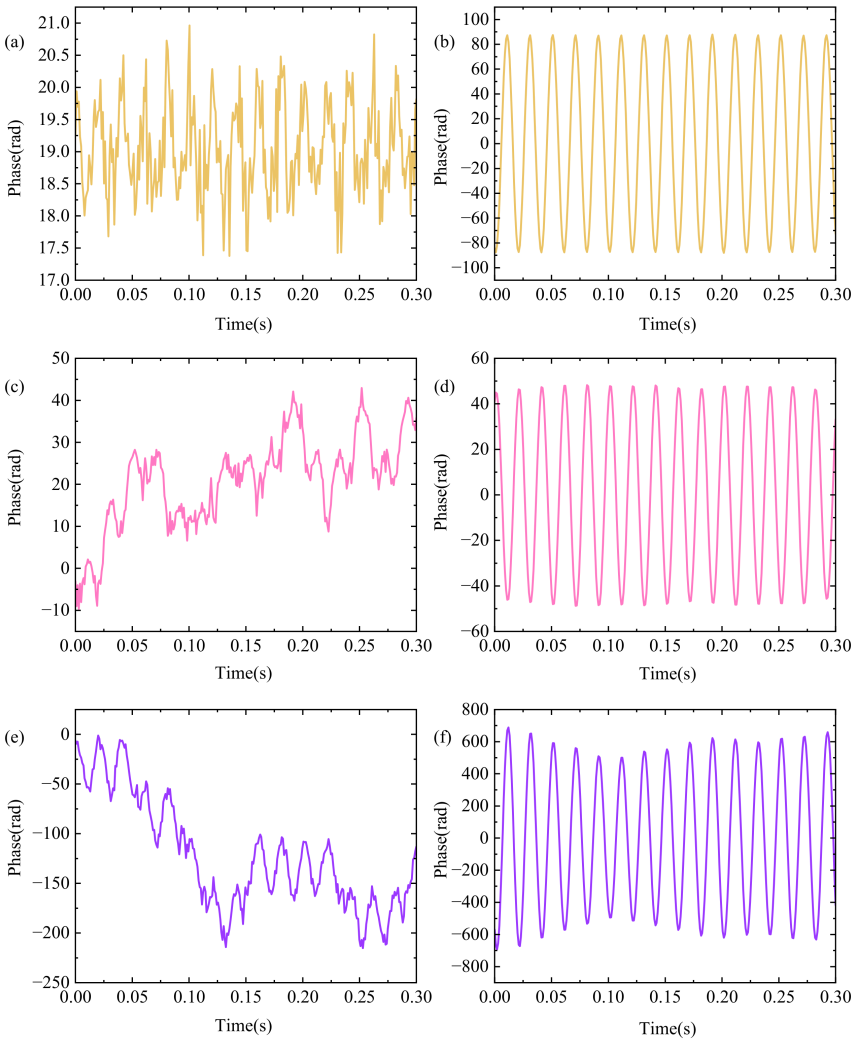


Figure 5. Comparison chart of the VMD algorithm optimization before and after use at different sensing distances when the vibration frequency is 50 Hz. (**a**,**c**,**e**) represent the original phase recovery results; (**b**,**d**,**f**) are the phase recovery results corresponding to the measured distances after noise reduction by the VMD algorithm.

As shown in Figure 6, Figure 6a, Figure 6b, and Figure 6c represent the power spectral density at vibration frequencies of 50 Hz when the sensing distance is 5 km, 10 km, and 30 km, respectively. From the thumbnail, it can be concluded that the system can demodulate the vibration signal at 30 km at a vibration frequency of 50 Hz, with the signal-to-noise ratios being 13.69 dB, 13.21 dB, and 11.66 dB, respectively.

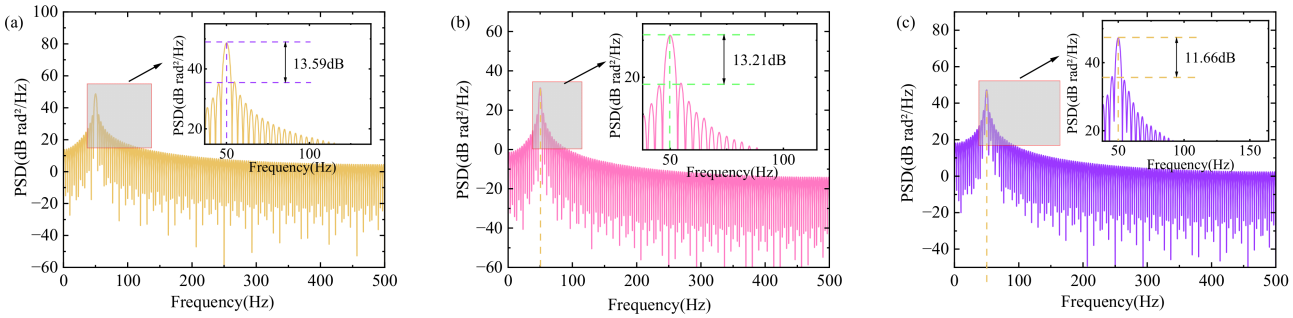


Figure 6. Power spectral density of phase at different sensing distances when the vibration frequency is 50 Hz. (**a**–**c**): the power spectral density diagrams for sensing distances of 5 kilometers, 10 kilometers, and 30 kilometers respectively.

3.2. Long-Distance Hertz-Level Vibration Detection Results and Analysis

Figure 7 provides a comparative visualization of phase recovery performance, highlighting the clear discrepancies between unprocessed raw signals and VMD-optimized results at a 30 km sensing distance. Specifically, Figure 7a, Figure 7c, and Figure 7e correspond to the original phase recovery waveforms for vibration frequencies of 1 Hz, 10 Hz, and 50 Hz, respectively, while Figure 7b, Figure 7d, and Figure 7f depict the phase recovery waveforms after VMD-based optimization at the same three frequencies. The vibration acquisition duration is uniformly set to 0.3 s across all test cases. It is evident from the figure that the VMD algorithm enables precise reconstruction of the target vibration waveform.

Figure 8 depicts the power spectral density (PSD) profiles associated with distinct vibration frequencies at a 30 km sensing range. Figure 8a, Figure 8b, and Figure 8c correspond to test scenarios with vibration frequencies of 1 Hz, 10 Hz, and 50 Hz, respectively. As a fundamental metric, the PSD characterizes the distribution of signal power across the frequency domain. Analysis of Figure 8 reveals that the proposed system can successfully demodulate vibration signals down to 1 Hz at a 30 km sensing distance, with the corresponding SNR measured as 11.78 dB, 16.27 dB, and 11.69 dB for the three frequencies, respectively.

3.3. Long-Distance Sub-Hertz Level Vibration Detection Results and Analysis

To validate the efficacy of the proposed algorithm in optimizing the demodulation of sub-Hertz vibration signals, a series of controlled experiments was conducted under a 30 km sensing distance. Vibration signals of 0.6 Hz and 0.8 Hz were applied on a 30 km optical fiber. The phase restoration before and after VMD optimization is shown in the figure. Figures 9a and 9b are the phase restoration results of the original signal and the VMD algorithm optimization result when applying a 0.6 Hz vibration, respectively. Figures 9c and 9d are the phase restoration results of the original signal and the VMD algorithm optimization result when applying a 0.8 Hz vibration, respectively. By comparison, the phase restoration results after VMD optimization significantly improved in the sub-Hertz frequency range.

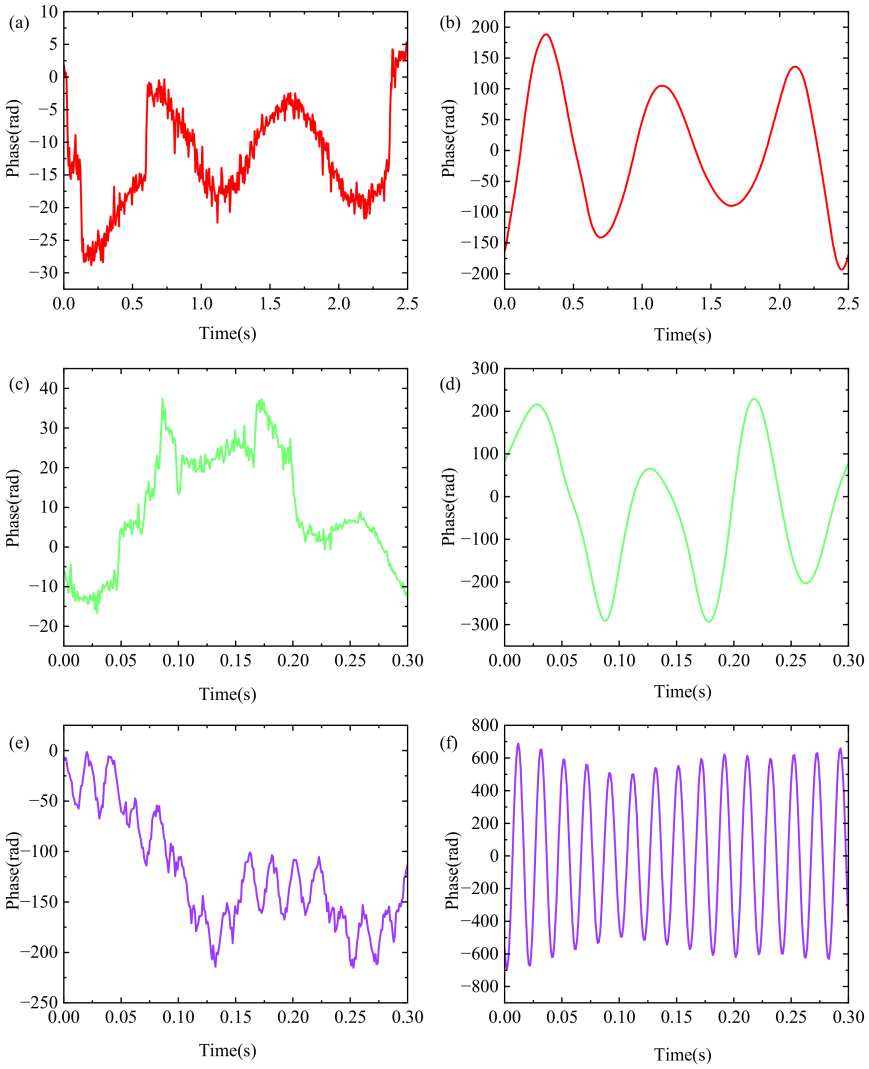


Figure 7. Comparison before and after optimization using the VMD algorithm when applying vibrations of different frequencies at a sensing distance of 30 km. (**a**,**c**,**e**) represent the original phase recovery results; (**b**,**d**,**f**) are the phase recovery results corresponding to the measured distances after noise reduction by the VMD algorithm.

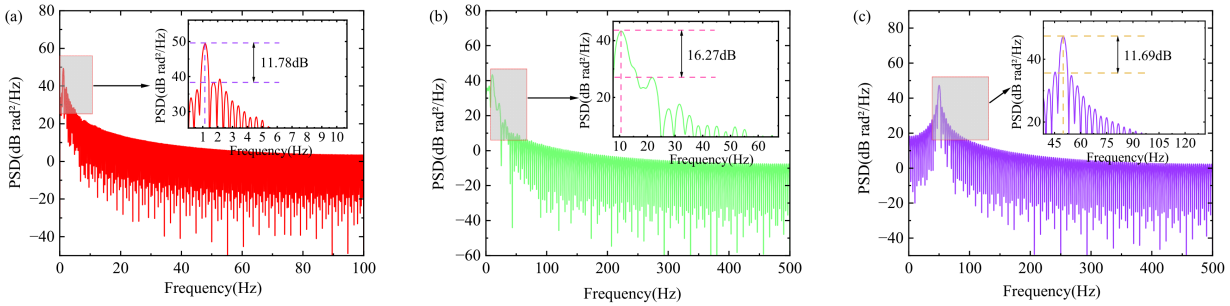


Figure 8. Power spectral density of phase at different vibration frequencies over a sensing distance of 30 km. (**a**–**c**): the power spectral density diagrams at vibration frequencies of 1 hertz, 10 hertz and 50 hertz respectively.

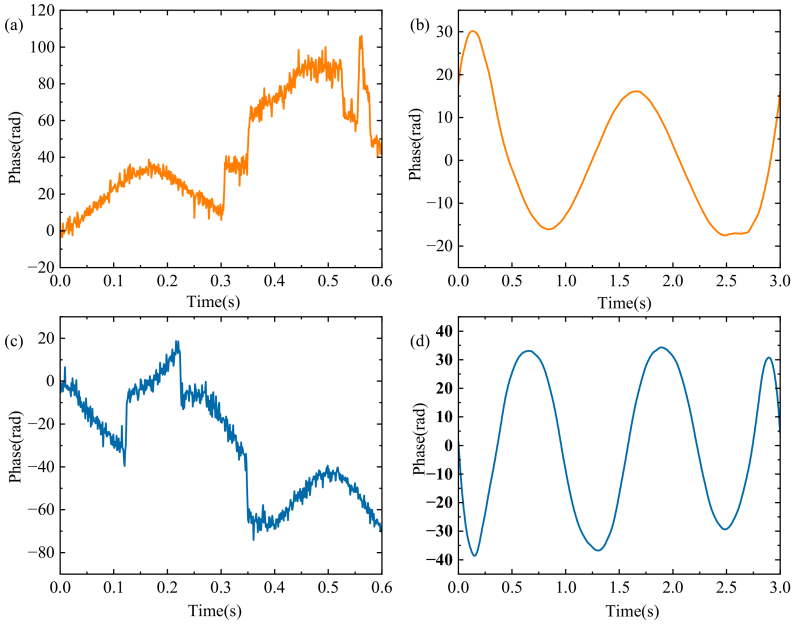


Figure 9. Comparison of phase restoration before and after optimization of vibration signals in the sub-Hertz frequency band (0.6 Hz, 0.8 Hz) with a sensing distance of 30 km. (**a**,**c**) represent the original phase recovery results; (**b**,**d**) are the phase recovery results corresponding to the measured distances after noise reduction by the VMD algorithm.

Figures 10a and 10b show the power spectral density curves of the demodulated phase under the application of 0.6 Hz and 0.8 Hz vibrations, respectively. It is evident from the experimental figures that the SNR of the demodulated phase corresponding to the two frequencies is 10.19 dB and 10.79 dB, respectively.

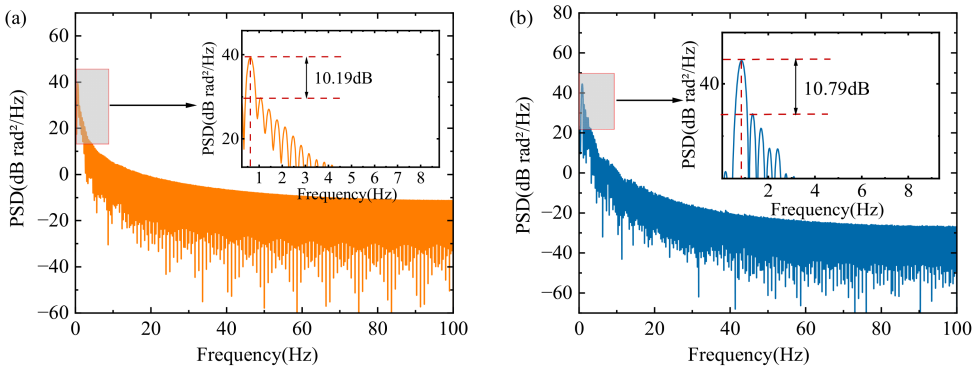


Figure 10. Power spectral density curves of the vibration signals with different frequencies applied. (**a**) and (**b**) are respectively the power spectral density diagrams at vibration frequencies of 0.6 hertz and 0.8 hertz.

4. Discussion

This paper focuses on two core issues in the coherent detection Φ-OTDR system: polarization fading suppression and phase demodulation noise optimization. It proposes an integrated scheme of polarization diversity reception combined with variational mode decomposition, which achieves high stability and accuracy in the detection of long-distance, low-frequency, and sub-Hertz vibration signals.

The existing polarization fading suppression methods mainly include active polarization control, polarization deflection, digital signal processing, and fiber structure optimization. Although they alleviate the problem of signal amplitude fading to some extent, they generally only improve signal strength while ignoring phase distortion and have

insufficient adaptability to long-distance low-frequency scenarios. At the same time, the non-stationary and nonlinear low-frequency phase drift introduced by laser frequency drift is difficult to effectively separate using traditional filtering methods. The multi-path noise superposition and signal–noise cross-terms brought by polarization diversity reception will further reduce the system's signal-to-noise ratio, restricting the accuracy of phase extraction and low-frequency detection capability. In this context, how to solve polarization fading while achieving noise suppression and low-frequency phase drift correction plays a pivotal role in enhancing the overall performance of the system

This study constructs a system combining polarization fading suppression, noise adaptive suppression, and correction of low-frequency phase deviations. The measured results effectively verify the previous research hypothesis: polarization diversity reception can eliminate the attenuation of beat frequency signals caused by polarization state mismatch at the optical path level. On this basis, the VMD algorithm, with its adaptive variational decomposition characteristics, can decompose the nonlinear and non-stationary demodulation phase signal into multiple independent mode components with different central frequencies, achieving precise separation of additional noise and target vibration signals, suppressing the noise base and optimizing the power spectral density. Experiments show that the proposed scheme can achieve stable signal restoration at different sensing distances of 5 km, 10 km, and 30 km, and complete high-precision phase demodulation of wide-frequency vibration ranging from 0.6 Hz, 0.8 Hz sub-Hertz level to 1 Hz, 10 Hz, 50 Hz Hertz level at 30 km distance, breaking through the detection bottleneck of traditional Φ-OTDR in long-distance, low-frequency, and weak signal scenarios.

This research is applicable to long-distance and multi-band distributed vibration sensing in polarization diversity Φ-OTDR systems. At the engineering application level, this scheme has important practical value in scenarios such as remote safety surveillance for oil and gas transmission pipelines, condition evaluation of large-scale infrastructures, perimeter security, and weak signal detection in geology. Compared to traditional schemes that rely on high-speed polarization controllers, special fibers, or complex modulation devices, it has higher stability and stronger potential for engineering implementation. In the future, the VMD algorithm parameters' adaptive ability and robustness can be further optimized for complex and strong interference environments. The algorithm's real-time performance can be enhanced by combining lightweight networks or hardware acceleration. The study of multi-physical field interference coupling mechanisms such as temperature, strain, and time-varying birefringence to expand the application scope is also planned. Integration with technologies such as deep learning noise reduction and Kalman filtering is explored to develop a more efficient multi-modal noise suppression framework, continuously improving the system's signal-to-noise ratio and phase demodulation accuracy.

5. Conclusions

This paper addresses the issues of signal instability caused by polarization fading in coherent detection Φ-OTDR systems, as well as extraneous noise interference and vibration demodulation problems introduced by polarization diversity reception. It adopts a joint scheme of polarization diversity reception and VMD, which not only solves the problem of polarization state fading from the optical path architecture but also realizes the phase restoration of effective vibration signals through the VMD algorithm.

The physical essence of the frequency modulation signal fading is clarified, the signal–noise mathematical model of polarization diversity reception is constructed, and the deterioration law of SNR is quantitatively derived. The theoretical framework of multi-scale VMD for suppressing LFD is constructed, and its feasibility in removing the low-frequency drift of LFD, system noise, and target vibration signals is demonstrated. Tests for phase

demodulation and PSD optimization at different transmission distances and vibration frequencies were completed. Phase restoration and PSD optimization tests were conducted for three typical transmission distances of 5 km, 10 km, and 30 km under 50 Hz excitation, as well as for the longest distance of 30 km at 1 Hz, 10 Hz, 50 Hz, and 0.6 Hz, 0.8 Hz sub-Hertz levels of vibration. In the above three cases, the maximum signal-to-noise ratio was increased to 13.59 dB, 16.27 dB, and 10.79 dB, respectively. The effectiveness of the proposed scheme in mitigating polarization fading is verified by the experimental results originating from fiber birefringence at diverse sensing ranges and vibration frequencies, enabling faithful recovery of the phase characteristics of the measured vibration signals.

Author Contributions: Conceptualization, R.M., W.B., Y.W. and B.J.; methodology, R.M., Y.W. and B.J.; software, R.M. and X.Z.; validation, R.M., W.B. and X.Z.; formal analysis, Y.W. and B.J.; investigation, R.M., Y.W. and B.J.; resources, Y.W. and B.J.; data curation, R.M., W.B., X.Z. and J.W.; writing—original draft preparation, R.M.; writing—review and editing, R.M., W.B., Y.W. and B.J.; visualization, R.M.; supervision, Y.W. and B.J.; project administration, B.J.; funding acquisition, Y.W. and B.J. All authors have read and agreed to the published version of the manuscript.

Funding: This work was supported in part by the Key Research and Development (R&D) Projects of Shanxi Province (grant no. 202402100101003), and in part by the Guiding Funds of Central Government for Supporting the Development of Local Science and Technology (grant no. YDZJSX2024C002).

Data Availability Statement: The data that support the findings of this study are available from the corresponding author upon reasonable request.

Conflicts of Interest: The authors declare no conflicts of interest.

References

1. Lu, Y.; Zhu, T.; Chen, L.; Bao, X. Distributed Vibration Sensor Based on Coherent Detection of Phase-OTDR. *J. Light. Technol.* **2010**, *28*, 3243–3249. [CrossRef]
2. Li, J.; Wang, Y.; Xiao, L.; Liu, X.; Jin, B. SNR enhancement with a non-local means image-denoising method for a Φ-OTDR system. *Appl. Opt.* **2023**, *62*, 2283–2291. [CrossRef]
3. Yu, Z.; Lu, Y.; Hu, X.; Meng, Z. Polarization dependence of the noise of phase measurement based on phase-sensitive OTDR. *J. Opt.* **2017**, *19*, 125602. [CrossRef]
4. Zhang, Y.; Zeng, H.; Su, C.; Yang, J.; Zhu, J.; Wang, J. Lightweight Vision Transformer for Real-Time Threat Level Assessment in Φ-OTDR-Based Pipeline Monitoring. *Appl. Sci.* **2026**, *16*, 1664. [CrossRef]
5. Zhang, Y.; Xu, Y.; Shan, Y.; Sun, Z.; Zhu, F.; Zhang, X. Polarization dependence of phase-sensitive optical time-domain reflectometry and its suppression method based on orthogonal-state of polarization pulse pair. *Opt. Eng.* **2016**, *55*, 074109. [CrossRef]
6. Demise, A.; Pasquale, D.; Muanenda, Y. Strategies for mitigating polarization fading in a DAS with homodyne detection and delayed self-mixing. *J. Phys. Photonics* **2025**, *7*, 045035. [CrossRef]
7. Wang, Y.; Xiao, L.; Li, Y.; Liang, B.; Liu, X.; Bai, Q.; Zhang, H.; Gao, Y.; Jin, B. Polarization-fading suppression of Φ-OTDR with Rayleigh gray-scale pattern aggregation method. *Appl. Opt.* **2021**, *60*, 10429–10436. [CrossRef]
8. Chen, C.; Liu, K.; Jing, J.; Hu, X.; Xue, K.; Zhang, D.; Du, Z.; Li, G.; Xu, T.; Jiang, J.; et al. Enhancing weak disturbance localization in asymmetric optical fiber vibration sensing system based on polarization control. *Opt. Lasers Eng.* **2025**, *195*, 109249. [CrossRef]
9. Wu, X.; Sun, A.; Liu, Y.; Ji, W. Digitalized Polarization Fading Suppression and Phase Demodulation Scheme of Phase-Sensitive Optical Time-Domain Reflectometry Based on Polarization Diversity Virtual Coherence. *Photonics* **2025**, *12*, 375. [CrossRef]
10. Wei, K.; Li, F.; Ji, Z.; Yan, W.; Shao, K.; Cong, Z.; Chen, P. Fading suppression method based on multi-core optical fiber bidirectional sensing loop for Φ-OTDR system. *Opt. Commun.* **2025**, *596*, 132534. [CrossRef]
11. Zhang, X.; Wang, Q.; Xiong, F.; Zhang, D.; Chen, M.; Chen, X.; Ding, Z.; Zhang, Y.; Zhou, T.; Wang, F.; et al. Performance enhancement method for phase-sensitive optical time-domain reflectometer system based on suppression of fading induced false alarms. *Opt. Eng.* **2020**, *59*, 046101. [CrossRef]
12. Li, Y. Influence of laser wavelength instability, polarization fading and phase fluctuation on local heterodyne detection wavelength scanning BOTDR. *Optoelectron. Lett.* **2023**, *19*, 200–204. [CrossRef]
13. Sandah, F.; Dossou, M.; Kinet, D.; Dandu, P.; Wuilpart, M. Study and mitigation of polarization fading in FBG-assisted direct-detection φ-OTDR. *Opt. Express* **2025**, *33*, 10873–10885. [CrossRef] [PubMed]

14. Lebedev, V.; Petrov, N.; Parfenov, V.; Velichko, E.N.; Shamray, A.V. Comparison of Polarization Fading Compensation Methods for Broadband Microwave Photonic Links by Introduced Noise and Achievable Dynamic Range. *Tech. Phys.* **2024**, *68*, 643–647. [CrossRef]
15. Mou, T.; Zhu, Y.; Lin, C.; Zou, C.; Xie, D.; Zhu, Y.; Dang, F.; Yuan, Y.; Gao, F.; Yang, J. Suppression of wavelength-dependent polarization fading using hybrid-polarization scheme in OFDR. *Opt. Express* **2024**, *32*, 1552–1561. [CrossRef]
16. Wang, P.; Li, Y.; Pang, X.; Du, H.; Wang, Z.; Yue, W.; Liu, M.; Zhang, S.; Liang, L.; Chen, B.; et al. Integrated polarization-diverse FMCW LiDAR with real-time CFAR for high-reliability long-range detection. *Opt. Express* **2026**, *34*, 7415–7428. [CrossRef]
17. Liu, B.; Wang, M.; Xia, F. SFOA-VMD-PE algorithm for a φ-OTDR detection system. *Appl. Opt.* **2025**, *64*, 9064–9071. [CrossRef]
18. Wu, H.; Jing, S.; Zhang, R.; Zhang, F.; Jiang, C. Phase unwrapping error identification and suppression method in φ-OTDR systems based on PELT-VMD-ARIMA. *Opt. Express* **2024**, *32*, 29344–29361. [CrossRef]
19. Chen, J.; Xing, H.; Liu, M.; Lv, X.; Zhang, L.; Chu, J.; Song, Y.; Yang, L. An optimised variational mode decomposition method based on improved coati optimisation algorithm for blockage detection of natural gas pipelines. *Nondestruct. Test. Eval.* **2026**, *41*, 1822–1860. [CrossRef]
20. Lv, Y.; Wang, P.; Wang, Y.; Liu, X.; Bai, Q.; Li, P.; Zhang, H.; Gao, Y.; Jin, B. Eliminating phase drift for distributed optical fiber acoustic sensing system with empirical mode decomposition. *Sensors* **2019**, *19*, 5392. [CrossRef]
21. Chen, C.; Liu, K.; Jing, J.; Hu, X.; Xue, K.; Zhang, D.; Du, Z.; Li, G.; Xu, T.; Jiang, J.; et al. Wide-Frequency vibration positioning of asymmetric interferometers based on dual endpoint detection and iterative VMD. *Opt. Laser Technol.* **2025**, *187*, 112882. [CrossRef]

Disclaimer/Publisher's Note: The statements, opinions and data contained in all publications are solely those of the individual author(s) and contributor(s) and not of MDPI and/or the editor(s). MDPI and/or the editor(s) disclaim responsibility for any injury to people or property resulting from any ideas, methods, instructions or products referred to in the content.